New Journal of Physics
The open access journal at the forefront of physics

Deutsche Physikalische Gesellschaft DPG IOP Institute of Physics

PAPER • OPEN ACCESS

Ultra-subwavelength resonators for high temperature high performance quantum detectors

To cite this article: Daniele Palaferri *et al* 2016 *New J. Phys.* **18** 113016

New Journal of Physics
The open access journal at the forefront of physics

Deutsche Physikalische Gesellschaft DPG
IOP Institute of Physics

Published in partnership with: Deutsche Physikalische Gesellschaft and the Institute of Physics

OPEN ACCESS

RECEIVED
20 May 2016

REVISED
3 October 2016

ACCEPTED FOR PUBLICATION
10 October 2016

PUBLISHED
8 November 2016

PAPER

Ultra-subwavelength resonators for high temperature high performance quantum detectors

Daniele Palaferri[1], **Yanko Todorov**[1], **Alireza Mottaghizadeh**[1], **Giulia Frucci**[1], **Giorgio Biasiol**[2] **and Carlo Sirtori**[1]

[1] Laboratoire Matériaux et Phénomènes Quantiques, Université Paris Diderot, Sorbonne Paris Cité, CNRS-UMS 7162, F-75013 Paris, France
[2] IOM CNR, Laboratorio TASC, Area Science Park, I-34149 Trieste, Italy

E-mail: daniele.palaferri@univ-paris-diderot.fr

Keywords: antennas, metamaterials, resonators, quantum wells, photoelectric conversion, gold

Abstract

In this article we have investigated two important properties of metallic nano-resonators which can substantially improve the temperature performances of infrared quantum detectors. The first is the antenna effect that increases the effective surface of photon collection and the second is the subwavelength metallic confinement that compresses radiation into very small volumes of interaction. To quantify our analysis we have defined and discussed two figures of merit, the *collection area* A_{coll} and the *focusing factor F*. Both quantities depend solely on the geometrical parameters of the structure and can be applied to improve the performance of any detector active region. In the last part, we describe three-dimensional electronic nano-resonators that provide highly subwavelength confinement of the electromagnetic energy, beyond the microcavity limits and illustrate that these device architectures have a tremendous potential to increase the temperature of operation of infrared quantum detectors.

Plasmonic nanostructures constitute an important and attractive research topic in the domain of photonics and nano-electronics [1, 2]. They are widely investigated in different ranges of the electromagnetic spectrum, starting from the visible [3, 4], through the infrared [5, 6] and down to the terahertz frequencies [7, 8]. Plasmonic nanostructure have been already exploited as an efficient mean to compress light in a sub-wavelength region of the space [7, 9] in order to improve the performances of optoelectronic devices, both as efficient absorbers [10–19] or emitters [20–23]. In particular, a fundamental property of a resonant absorber, such as plasmonic nanoparticle, is its ability to gather photons from a collection area A_{coll} that can be much larger than its geometrical cross section σ [24], as illustrated in figure 1. The ultimate limit of this phenomenon is found in the quantum transition of a single atom at the resonant wavelength λ, where A_{coll} can be identified with an absorption cross section $A_{\mathrm{coll}} = 3\lambda^2/4\pi$ [25]. While this concept is widely used in antenna-coupled devices in the low-frequency part of the electromagnetic spectrum [26], it is clearly underexploited for infrared and optical quantum detectors of radiation. In particular, we have recently illustrated that in the mid-infrared and THz frequencies ranges, antenna-coupled quantum well infrared photo-detectors (QWIPs) can lead to a substantial reduction of the dark current with respect to the photocurrent signal [15, 16]. High temperature, high performance photo-detectors in the mid- and far- infrared is an actual issue that would enable the realization of sensitive thermal imaging setups with a broad range of applications [27]. Resonant structures, such as cavities and photonic cristals have already been envisioned for the enhancement for both intrasubband [28] and intersubband photo-detectors [20, 29], however in these studies the antenna effect was not taken into account.

In the current work, we provide a quantitative discussion on how nanoresonator arrays can impact the performance of quantum detectors in terms of responsivity, detectivity and background limited thermal performance. The improvement of the detector performance is expressed in terms of the collection area A_{coll} of the nanostructure, seen as an antenna, and the local field enhancement factor F, which will be introduced below (equation (7)). These quantities are universal figures of merit, in the sense that they can be adapted to any kind of

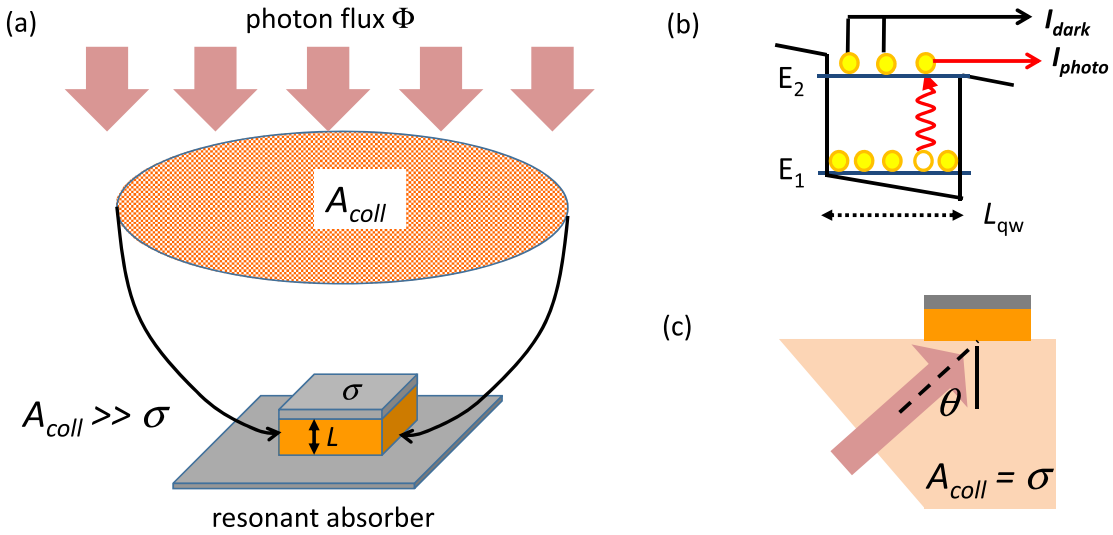

Figure 1. (a) A general scheme of a detector which comprises a resonant absorber embedded in a metallic nanoresonator. Thanks to the antenna function of the resonator, photons are gathered on a collection area A_{coll} that can be much larger than the detector cross section σ. The quantity σ indicates the number of photons incident on the structure per unit surface and unit time. (b) A resonant absorber based on the confined subbands in semiconductor quantum well of a thickness L_{qw}, typical for a QWIP. For simplicity, the in-plane parabolic dispersion is not indicated. Electrons are promoted from the first level E_1 to the second E_2 either by photo-absorption (photocurrent I_{phot}) or thermal excitation (dark current I_{dark}). (c) A standard geometry for the characterizations of absorbing regions based on quantum wells. The photon flux is coupled into the absorber through the angle-polished facet of the semiconductor substrate. In that case, the photon absorption area A_{coll} coincides with the geometrical cross section σ.

nanostructures and absorbing regions. The detector optimization, following the guidelines of our figures of merit, will lead us to a resonator architectures where the electric field is confined in nano-metric volumes, with strong potential for high temperature, high performance THz quantum detectors.

In figure 1(a) we have presented a general scheme for a detector built with a metallic resonator of geometrical cross section σ. For our discussion, we shall consider the specific case of unipolar intersubband detectors such as QWIP. We suppose that the absorbing region of the detector ('resonant absorber' as indicated in figure 1(a)) is made, for instance, of a two-level semiconductor quantum well with subband energies E_1 and E_2, as depicted in figure 1(b). A typical example of photonic structure of such detector is a double-metal patch resonator, which acts both as a microcavity and an antenna [26, 31]. Let Φ be the number of photons incident per unit surface and unit time on the structure. We define an area A_{coll}, larger than the geometrical cross section σ, such that the number of photons absorbed by the detector per unit time are exactly equal to $A_{coll}\,\Phi$. The total current produced in the detectors then comprises a photocurrent I_{photo}, and a thermally activated dark current I_{dark}:

$$I_{photo} = RA_{coll}\Phi E_{21} \tag{1}$$

$$I_{dark}(T) = \sigma J_0 T \exp(-E_{act}/k_B T) \tag{2}$$

Here R is the internal responsivity of the detector, J_0 is a constant that depends solely on the properties of the absorbing region [26], E_{act} is an activation energy that in most cases can be identified with the energy of the quantum transition $E_{21} = E_2 - E_1$, and k_B is the Boltzmann constant. In the following, we will assume that the electromagnetic mode of the metallic nano-structure has a resonant frequency f_{res} that is always matched with the frequency of the quantum transition, $f_{res} = E_{21}/\hbar$. When the photon flux arises from the thermal emission of a 300 K background, we can define an important figure of merit, which is the background limited performance (BLIP) temperature of the detector, T_{BLIP} [26]. This quantity is inferred from the temperature dependence of the dark current equation (2) through the condition $I_{photo} = I_{dark}(T_{BLIP})$. The value of T_{BLIP} sets the temperature above which the detectivity is limited by the dark current. Below T_{BLIP} the noise properties are imposed by the photocurrent from the 300 K background and no detectivity improvement can be obtained by lowering the temperature of operation. Typical values of T_{BLIP} for intersubband detectors are 70 K for resonant wavelength around 9 μm [33, 34] and much lower (10 K–17 K) for detectors operating at THz frequencies [35]. This decrease of the performance can be easily deduced from equation (2) where $E_{act} \sim E_{12}$ scales with the energy separation between levels 1 and 2 [36].

The benefit from the antenna effect is apparent immediately from equation (1) as the photo-current I_{photo} is proportional to the photon collection area A_{coll}, and the dark current to the geometrical cross section σ. In that sense, the areas A_{coll} and σ can be identified as the 'photonic' and 'electric' area of the detector [27]. Therefore, in the case where $A_{coll} \gg \sigma$ the photocurrent signal is enhanced with respect to the dark current, leading to a

higher T_{BLIP} [15, 16, 37]. Note that so far, intersubband devices have been essentially implemented in the regime where $A_{\mathrm{coll}} = \sigma$, with some exceptions [7, 8, 30].

Using the model from reference [15], the internal responsivity R of the structure, which is defined in equation (1) can be expressed as:

$$R = B_{isb} Q \frac{eg}{N_{qw} E_{21}} \tag{3}$$

The term 'internal' is used in the sense that the photocurrent has been normalized on the number of photons coupled into the device, in accordance with the definition of A_{coll} from equation (1). Here Q is the quality factor of the resonant structure and the coefficient B_{isb} describes analogously the fraction of the electromagnetic field absorbed by the quantum transition, and averaged per cycle of oscillation, normalized on the total number of photons stored in the cavity. The quality factor Q thus has three contributions: $1/Q = B_{\mathrm{isb}} + 1/Q_{\mathrm{rad}} + 1/Q_{\mathrm{nr}}$, with Q_{rad} describing the radiation loss of the resonator, owe to its coupling with the free space radiation, and Q_{nr} describes all non-radiative loss channels (i.e. loss in the metal) other than the resonant QWIP absorption described by B_{isb}. The parameter g is the photo-absorption gain (number of electrons generated per photon absorbed), and e is the electron charge. Using the results from [15], the coefficient $B_{\mathrm{isb}}(E)$ can be expressed as a function of the energy E of the incident photons:

$$B_{isb}(E) = f_w \frac{E_P^2}{4E_{21}} \frac{\hbar\Gamma}{(E - E_{21})^2 + \frac{(\hbar\Gamma)^2}{4}} \tag{4}$$

Here $\hbar\Gamma$ is the linewidth of the quantum transition, E_{P} is the plasma frequency that depends on the number of available carriers for photo-absorption [15], and f_{w} is the geometrical overlap between the electric field of the nano-structure and the quantum absorbing region in the direction perpendicular to the surface of the device. In the case of a double-metal structure, as described in figure 1(a), it can be expressed as $f_{\mathrm{w}} = N_{\mathrm{qw}} L_{\mathrm{qw}}/L$, with L the thickness of the double-metal structure (figure 1(a)), L_{qw} the thickness of the quantum well and N_{qw} the total number of quantum wells inserted the metallic structure.

In order to evaluate the impact of the geometrical layout from figure 1(a) we compare it to a standard substrate-coupled geometry, also referred as '*mesa*', depicted in figure 1(c). The mesa configuration is used to characterize the detector absorbing region alone [38]. In this configuration the incident photons are coupled through the angle-polished facet of the semiconductor substrate. To recover the standard definition of the photocurrent in this case [30], we assume that the quantity A_{coll} coincides with physical detector dimensions, $A_{\mathrm{coll}} = \sigma$. The photocurrent is then expressed as $I^0_{\mathrm{photo}} = tR_0\sigma\Phi E_{21}$, where t is the transmission coefficient of the facet, and $R_0 = \eta\, eg/(N_{qw} E_{21})$ is the intrinsic responsivity of the QWIP. Here η is the absorption quantum efficiency of the transition [36]. The BLIP temperature of the mesa T^0_{BLIP} is defined as $I^0_{\mathrm{photo}} = I_{\mathrm{dark}}(T^0_{\mathrm{BLIP}})$, and depends solely on the quantum design of the absorbing region and the properties of the semiconductor material, but not on the device cross section σ. Using the expression of the quantum efficiency η from [36] we obtain the following relation:

$$B_{isb}(E) = \eta(E) \frac{\cos\theta}{\sin^2\theta} \frac{\lambda_{21}}{2\pi L} \tag{5}$$

Here, θ is the incident angle in figure 1(c) that shall be considered $\theta = 45°$ as usually found in experiments, and $\lambda_{21} = \hbar c/E_{21}$ is the resonant wavelength. Combining all definitions stated above, we arrive at the following link between the BLIP temperature T_{BLIP} of the antenna-coupled structure as a function of T^0_{BLIP} of the reference sample described in figure 1(c):

$$T_{BLIP} = \frac{T^0_{BLIP}}{1 - \frac{k_b T^0_{BLIP}}{E_{21}} \left\{ \ln F - \ln K + \ln\left(\frac{T^0_{BLIP}}{T_{BLIP}} \right) \right\}} \tag{6}$$

In this formula we have defined two quantities F and K such as:

$$F = \frac{A_{coll}\lambda_{21}}{V} Q \tag{7}$$

where $V = \sigma L$ is the volume of the nano-structure, as shown in figure 1(a), and

$$K = \frac{2\pi\cos\theta}{\sin^2\theta} t \tag{8}$$

Equation (8) contains quantities that depend only on the mesa configuration. Taking GaAs substrate with a refractive index $n = 3.5$ and $\theta = 45°$ we have $t = 4n/(1+n)^2 = 0.7$ and the first term can be numerically evaluated at $\ln K = 1.82$.

Equation (6) indicates that the BLIP temperature of the detector can be increased if the factor F is increased by judicious of the geometry of the structure. This quantity, which is an important figure of merit for any detector architecture, has a straightforward interpretation in terms of the local electric field enhancement of the photonic resonator [39]. Indeed, let E_{out} be the electric field amplitude of the incident wave. Then the power flow density of the incident wave can be expressed as $\varepsilon_0 c|E_{out}|^2/2$. If E_{in} is the amplitude of the electric field stored inside the resonator, then the total energy density can be expressed as $\varepsilon_0\varepsilon|E_{in}|^2V/2$ with $\varepsilon = n^2$ (the factor ½ arises from cosine variation of the electric field along the patch [7]). We used the fact that the electric energy density $\varepsilon_0\varepsilon|E_{in}|^2V/4$ is equal to the magnetic energy density at resonance. Then the energy conservation dictates that $A_{coll}\varepsilon_0 c|E_{out}|^2/2 = \varepsilon_0\varepsilon|E_{in}|^2V/2 \times (Q/\omega_{res})$ with ω_{res} the angular frequency of the resonant mode, which leads to the equality: $\varepsilon|E_{in}|^2/|E_{out}|^2 = F/2\pi$. Because of this interpretation, the factor F shall be referred in the following as 'focusing factor', as it expresses quantitatively how the density energy of free space photons is compressed into the cavity volume V. It is remarkable that if we consider the case of a single elastically bound electron, we have $A_{coll} = 3\lambda_{21}^2/4\pi$, and then the factor $F/2\pi$ ultimately becomes the Purcell factor of the system. These considerations indicate that the definition (7) has a more general bearing than the particular case of intersubband detectors that we used to establish the results (6) and (7). Indeed, we expect that for other type of detectors the numerical constant ln$K$ will be different, yet of the order of unity, and the equation (6) will still hold.

Since, according to equation (6), the BLIP temperature T_{BLIP} has a logarithmic dependence on the focusing factor F, a substantial increase in the temperature performance can be achieved when F is varied through several orders of magnitude. From equation (7), the design parameters at hand are the collection area A_{coll}, the volume of the absorbing region V and the quality factor Q. This last term can be analyzed by comparing the intrinsic quality factor of the resonator Q_{cav}, defined from $1/Q_{cav} = 1/Q_{rad} + 1/Q_{nr}$ and the coefficient B_{isb}. Typically, in double-metal resonators with strongly subwavelength thickness we have $1/Q_{rad} \ll 1/Q_{nr}$ [7]. In the case of very low Q_{cav} cavities, a system too lossy with $1/Q_{cav} \gg B_{isb}$, the detector is inefficient as most of the incident photons are absorbed by the metal rather than the quantum transition. In the opposite regime, where $B_{isb} \gg 1/Q_{cav}$, all photons are absorbed by the quantum wells. This situation occurs in the case of very high Q_{cav} resonators (which could be, for example, photonic crystal resonators [30]). Notice that in this limit the responsivity R does not depend anymore on B_{isb} and the focusing factor becomes inversionally proportional to B_{isb}. There is no interest therefore in further increasing the rate of absorption as it will simply increase the noise due to the increase of photogenerated carries. In this counter-intuitive limit the high Q_{cav} cavity acts as a photon storage that 'slows down' the absorption in the active region, thus increasing the T_{BLIP}. Moreover, increasing the absorption would imply the use of heavily doped QWIPs [40, 41], which have a strong dark current and low BLIP temperature and detectivity. Optimum detector performance has been already established by relatively low doping levels: on the order of 10^{10} cm^{-2}–10^{11} cm^{-2} depending on the spectral region of operation [36]. The only degrees of freedom that are left to improve the photonic resonator that contains the absorbing region are the geometrical properties contained in the factor F defined in equation (7).

It has been experimentally and theoretically shown that arrays of resonators can feature a strong ability to absorb the incident radiation on a large cross-section [7, 42, 44]. Therefore, following the ideas developed in previous works [8, 15, 16, 45], we have analyzed diluted arrays of double-metal square patch-cavity resonators as a model system to illustrate the roles of the parameters A_{coll} and F. In that case $B_{isb} = 0$ and $Q = Q_{cav}$. For our analysis, we started by varying the filling factor of a set of arrays with identical patches as described in figure 2(a). The resonators are made of a 2 μm thick GaAs layer sandwiched between two metal plates. The patches have a lateral width of $s = 10$ μm, thus resonating at a frequency $f_{res} = c/(2n_{eff}s)$ around 4.5 THz, where $n_{eff} \sim 3.3$ the effective index of the confined mode [7]. The arrays are periodic with a square unit cell area $p^2 = \Sigma$. As shown in figure 2(a) the semiconductor material is dry-etched by inductively coupled plasma everywhere except under the square metal patch. While the area of the square patch is kept constant at 10×10 μm^2, we studied arrays with periods $p = 15$ μm, 25 μm, 35 μm, 55 μm and 80 μm (respective unit cells: $\Sigma = 225$ μm^2, 625 μm^2, 1225 μm^2, 3025 μm^2 and 6400 μm^2). In figure 2(b) we show the reflectivity spectra of the arrays, obtained with the Globar source of a Fourier Transform Interferometer at almost normal incidence (15° with respect to the array normal). The mode of the double-metal patch is revealed as a dip in the reflectivity spectra at the expected value $f_{res} = 4.5$ THz. Apart the quality factor Q and the resonant frequency f_{res}, the dip is characterized by its 'contrast' $C = 1 - \mathscr{R}_{min}$, with $\mathscr{R}_{min}$ the reflectivity minimum. The values of both C and Q, extracted from Lorentzian fits of the data are plotted as function of Σ in figure 2(c). Note that both C and Q depend strongly on the array periodicity, as previously observed with split-ring resonators [43] and patch wire cavities [8]. According to energy conservation, the contrast C provides the fraction of photons absorbed by the array at resonance. Since the number of incident photons per unit time on each element of the array is $\Phi\Sigma$, the collection element for each patch in the array is provided by the equation:

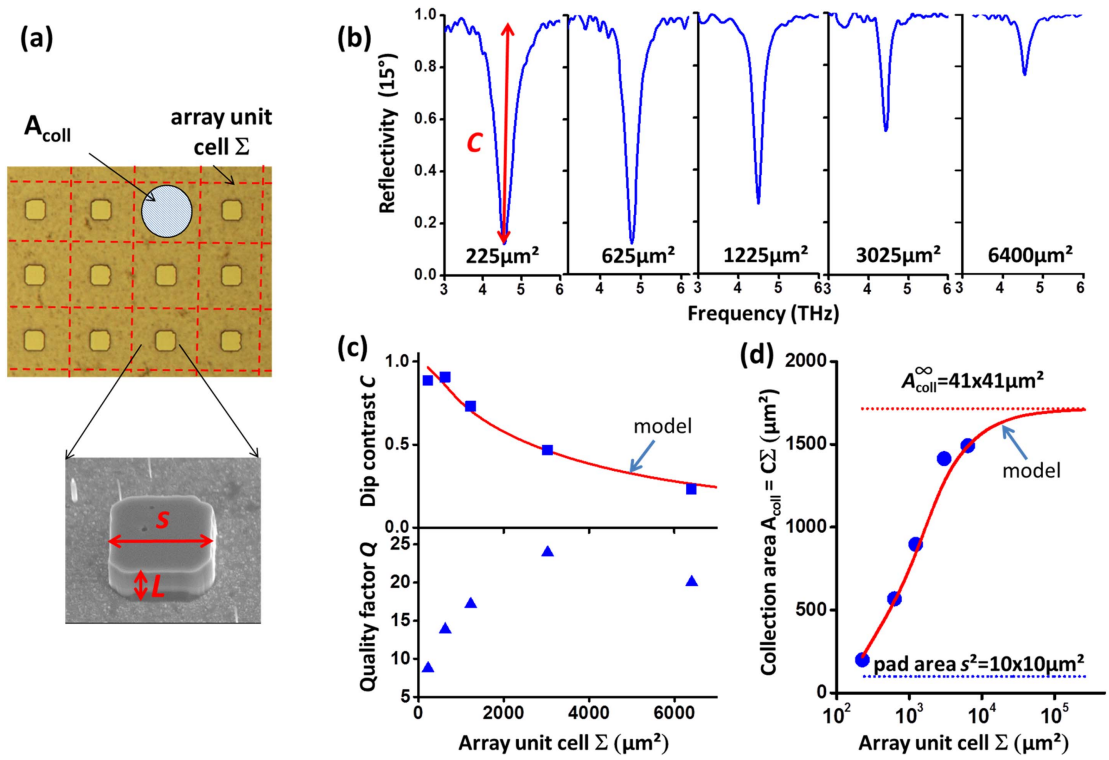

Figure 2. (a) Optical microscope picture of an array with square patch resonators (up) and a scanning electron microscope picture of a single element with thickness L and square side s (down). In the present case $L = 2$ μm and $s = 10$ μm. We have indicated the array unit cell surface Σ. The collection area $A_{\rm coll}$ for each resonator is expected to be somehow smaller or equal to Σ, as illustrated. (b) A set of reflectivity spectra for arrays with different square unit cells Σ, indicated for each spectrum. (c) Amplitude of the reflectivity dip C (also called 'dip contrast') and quality factor Q as a function of Σ. The dots are experimental data and the continuous line is the model from equation (10). (c) Individual collection area $A_{\rm coll}$ as a function of Σ. The dots are experimental data and the continuous line is the model. The upper dotted line shows the asymptotic value $A_{\rm coll}^{\infty}$ for a single resonator.

$$A_{\rm coll} = (1 - \mathscr{R}_{\rm min})\Sigma = C\Sigma \tag{9}$$

The reflectivity spectra therefore allow a direct determination of the collection area $A_{\rm coll}$ per element. This result has been plotted in figure 2(d) (dots). We can already notice that the typical values of $A_{\rm coll}$ are much larger than the cross section of the square pad (10×10 μm^2), up to 15 times in the measured values.

The remarkable behavior that is evident from the results in figure 2 is that, while the contrast C is optimum for dense arrays and decreases with the unit cell area Σ, the collection area $A_{\rm coll}$ increases monotonically with Σ and seems to saturate. We thus observe a rather counter-intuitive result that, when put together, the absorbing elements tend to decrease their individual absorption area. On the other side, the system as a whole has an optimum ability to absorb the incident radiation, when the contrast C reaches unity for a particular value of Σ (critical coupling point, [7]). To capture this behavior and to estimate the maximum value of $A_{\rm coll}$ in our system we rely on the analytical model described in [8], where we provided an explicit expression of peak contrast C as a function of Σ and the characteristics of the individual resonators:

$$C = \frac{4\alpha}{(1+\alpha)^2}, \quad \alpha = \frac{\lambda_{21}^2}{D_{rad}\Sigma}\frac{Q_{nr}}{Q_{rad}} \tag{10}$$

In this model, the effect of the radiation loss latter is evaluated according to the expression $Q_{\rm rad} = \lambda_{21}\pi n_{\rm eff}^2/(4LD_{\rm rad}) = 73$ [8] with $n_{\rm eff} = \lambda_{21}/2\,s = 3.3$, and thus $Q_{\rm rad}$ is typically one order of magnitude greater than $Q_{\rm nr}$. Using the values of the measured quality factor Q as a function of the unit cell area Σ (figure 2(c)) and our analytical model from equation (10) we obtained C as a function of Σ, as shown as a continuous curve in figure 2(c) (upper panel). The agreement between our model and the experiment is excellent, without any fit parameters, except for the denser array ($\Sigma = 225$ μm^2). The discrepancy at that point can be explained by near-field coupling between the resonators [45], which introduced additional linewidth broadening. Using our model, we can now provide an analytical expression for the collection area $A_{\rm coll}$ of the patch antenna array as defined in equation (9):

$$A_{coll} = \frac{A^1_{coll}(Q_{nr})}{\left(1 + \frac{A^1_{coll}(Q_{nr})}{4\,\Sigma}\right)^2},\ A^1_{coll}(Q_{nr}) = \frac{64}{\pi}\frac{V}{\lambda_{21}}Q_{nr} \tag{11}$$

Here $A^1_{coll}(Q_{nr})$ is the collection area obtained by letting $\Sigma \to \infty$ for a given quality factor Q_{nr} and as such it represents the collection area of a single element of the array. Note that the area A^1_{coll} is 4 times bigger than the area of the unit cell Σ at the critical coupling, i.e. when $C = 1$ and $4\Sigma = A^1_{coll}$. As seen from the data in figure 2(c) the quality factor has a strong dependence on Σ and therefore the asymptotic limit that provides the collection area of a single element is obtained as:

$$A^1_{coll}(Q_{nr})|_{\Sigma\to\infty} = A^\infty_{coll} = \frac{64}{\pi}\frac{V}{\lambda_{21}}Q^\infty_{nr} \tag{12}$$

with the Q^∞_{nr} the asymptotic limit of the non-radiative contribution in the quality factor for very diluted arrays, obtained from the data in figure 2(c). Equation (11) accounts well for the monotonic increase of the collection area observed in experiments, as shown in figure 2(d). It expresses the fact that the collection area per element is always smaller when elements are arranged in an array. Using our model, we can extrapolate the 'intrinsic' value of A^∞_{coll} to be 1717 μm^2 = 41 × 41 μm^2, almost 17 times larger than the cross section of the square pad. With the analytical expression of A^∞_{coll} we evaluate the maximum local field enhancement for the patch antenna geometry, for a volume $V = Ls^2$:

$$F^\infty = \frac{A^\infty_{coll}\lambda_{21}}{V}Q^\infty = \frac{64}{\pi}\frac{(Q^\infty_{nr})^2}{1+e} \tag{13}$$

Here, $e = Q^\infty_{nr}/Q_{rad}$ is the extraction efficiency of the resonator. It is remarkable that the limiting value F^∞ is completely independent from the aspect ratio of the resonator, and namely the resonator volume, but depends only on the resonator loss. This limit is intimately related to the fact that the patch antenna resonance relies on propagation effects, i.e. the lateral dimensions of the cavity are commensurable with the wavelength in the material. Indeed, the modes of these structures can be described as a standing–wave Fabri-Perot like resonances [7]. As the wavelength of the first order mode is provided by $\lambda_{21} = 2n_{eff}s$, the resonator dimensions cancel by combining equations (7) and (12). The same considerations can be easily shown to be valid for patch antenna resonators with an arbitrary cross sections. In particular, taking $Q^\infty_{nr} = \left(\frac{1}{Q^\infty} - \frac{1}{Q_{rad}}\right)^{-1} = 28$, we obtain from equation (13) a limiting value $F^\infty = 1.1 \times 10^4$. Let us considering the THz detector from [16], which operates at 5.4 THz and had a BLIP temperature $T^0_{\rm BLIP} = 17$ K. An activation energy $E_{\rm act} = 17.7$ meV was obtained by fitting the dark current as a function of the temperature with equation (2) from the data reported in [16]. These figures lead to a maximum achievable BLIP performance of $T^\infty_{BLIP} = 38\ K$ from equation (6).

As F^∞ is independent from the shape of the microcavity, and hence the resonant wavelength, we can use the above results to make predictions for infrared detectors operating in other ranges. For instance, our results can be extrapolated to the Mid-Infrared (MIR) range ($\lambda = 9$ μm), which is practically important for thermal imaging [36]. Typically, for a $\lambda = 9$ μm we have $T^0_{\rm BLIP} = 70$ K [34], and the quality factors are twice lower with respective to THz cavities, because of the increased metal loss [46]. Extrapolating these numbers to the MIR domain we obtain $F^\infty = 3 \times 10^3$ which provides $T^\infty_{BLIP} = 100$ K for a cavity-embedded QWIP detector at 9 μm.

From a practical point of view, it is important to compare the collection efficiency of the detector, seen as a single pixel, with the performance of the optical system, used, for instance, in an imaging array. Provided a wavelength of operation λ_{21}, the ultimate diffraction-limited spot has an area of the order of λ^2_{21}. This value is generally superior to the collection area of a single detector. Indeed, in the present geometry, using equation (12) the ratio $A^\infty_{coll}/\lambda^2_{21}$ is readily estimated at 0.4. Since it is practically difficult to achieve diffraction-limited spots, a natural solution is to use an array of elements that covers wide illuminated area. However, as shown from figure 2(d), this leads to a reduction of the individual collection area $A_{\rm coll}$ and hence a lower temperature performance. These considerations show that there is always some trade-off between the maximum temperature $T_{\rm BLIP}$ required and the overall collection ability of the detector array. This is further illustrated in figure 3, where we have shown both the BLIP temperature and the reflectivity contrast C as a function of the array unit cell surface Σ, assuming the same absorbing region as in [16]. This graph shows that the maximum temperature $T^\infty_{\rm BLIP} = 38$ K is obtained for $\Sigma = 3015$ μm (array period $p = 55$ μm), where the photon rejection rate is $1 - C = 57\%$, however the temperature drops only by less than one degree if the array is operated with 50% rejection rate. On the other hand, $T_{\rm BLIP}$ for a dense array operating at the critical coupling with $C = 1$ is equal to 25 K, still about 8 K higher than the intrinsic value $T^0_{\rm BLIP} = 17$ K.

A possible method to optimize $A_{\rm coll}$ is to use planar antennas, such as bow-tie or spiral have the ability to collect efficiently the incident radiation on areas larger than the diffraction limit [47, 48], however these structures are not naturally compatible with the intersubband selection rule. Alternative solutions have been proposed, such as the combination of planar antennas with patch microcavities [23], or exploring 'monopolar'

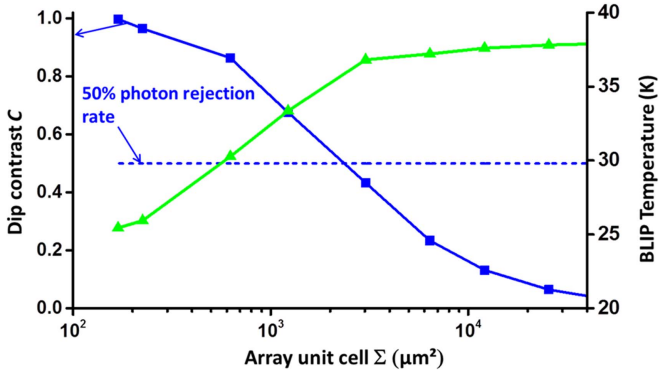

Figure 3. Plot of the peak contrast C and the BLIP temperature T_{BLIP} as a function of Σ, assuming an absorbing region resonant at 5.4 THz, as the one described in [16]. The dashed line indicates $C = 0.5$, which corresponds to a 50% of photon rejection rate.

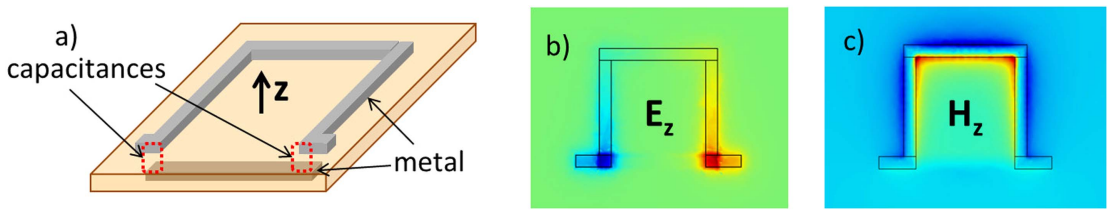

Figure 4. (a) Schematics of a three-dimensional metallic circuit-like resonator with a reduced volume of the capacitive regions. The resonant absorber is inserted in the capacitors. (b), (c) Numerical simulations of the electric field component E_z (b) and magnetic field component H_z (c) in the medium plane of the substrate. (d) The plot (b) shows the strong localization of the electric field in the capacitive parts.

resonators combined with loop antennas [49–51]. In the following, we propose another approach to increase the focusing factor of the array F, and hence the value of T_{BLIP} even for dense arrays, which adds degrees of freedom for the optimization of the system.

Since the fundamental limitation (equation (13)) in microcavities arises from propagation effects, a possible alternative is to explore electromagnetic resonators that are not subject to this limitations. A natural choice for such systems is the circuit resonators, which are used as building blocks of metamaterials in the high frequency part of the microwave spectrum [52]. Indeed, such resonators operate well below the propagation limit [53], and could therefore provide much higher focusing factors F. Such structures have been recently demonstrated specifically for intersubband THz devices [51, 54–60]. Typically, such circuit-like structure have a double-metal part, that plays the role of the capacitance, and an inductive part, that confines the magnetic field. In that case the volume V in the expression of the focusing factor (equation (7)) corresponds to the volume of the capacitance [61]. Note that this type of electromagnetic resonators could be implemented also at higher frequencies. However their fabrication could be already very challenging in the mid-infrared spectral region and extremely difficult in the near-ir/visible.

We recently proposed a three-dimensional architecture, which allows for an increased confinement of the THz electric field and is compatible with the selection rule of intersubband transitions [59]. Our design is recalled in figure 4(a). It consists of a thin metal strip instead of a continuous ground plate, a dielectric slab and a top metal loop. In figures 4(b) and (c) we present simulations of the electric E_z and magnetic H_z field of the structure in a plane that crosses the middle of the dielectric slab, with the z-axis is perpendicular to the plane of the slab. These simulations reveal that the electric field E_z is strongly confined in the regions of overlap between the top and bottom metals, while the magnetic field H_z is rather localized around the loop. The analysis presented in [59] allows to assign a capacitance C_{db} and an inductance L_{loop} as a function of the geometrical parameters of the structure. The resonant frequency is then obtained as $f_{res} = 1/2\pi\sqrt{C_{db}L_{loop}}$. This design allows therefore the reduction of the capacitive part by expending of the inductive one, while the resonant frequency f_{res} is kept constant [59]. In that case the capacitance volume V can be made much smaller than the resonant wavelength, resulting in a high focusing factor F, according to our definition equation (7).

To probe this concept experimentally, we realized structures with progressively shrinking capacitances while the inductive loops have been adjusted so that all structures resonate around 3 THz. For these proof of principle studies we used SiO_2 dielectric layers which simplified the fabrication process. Scanning electron microscope

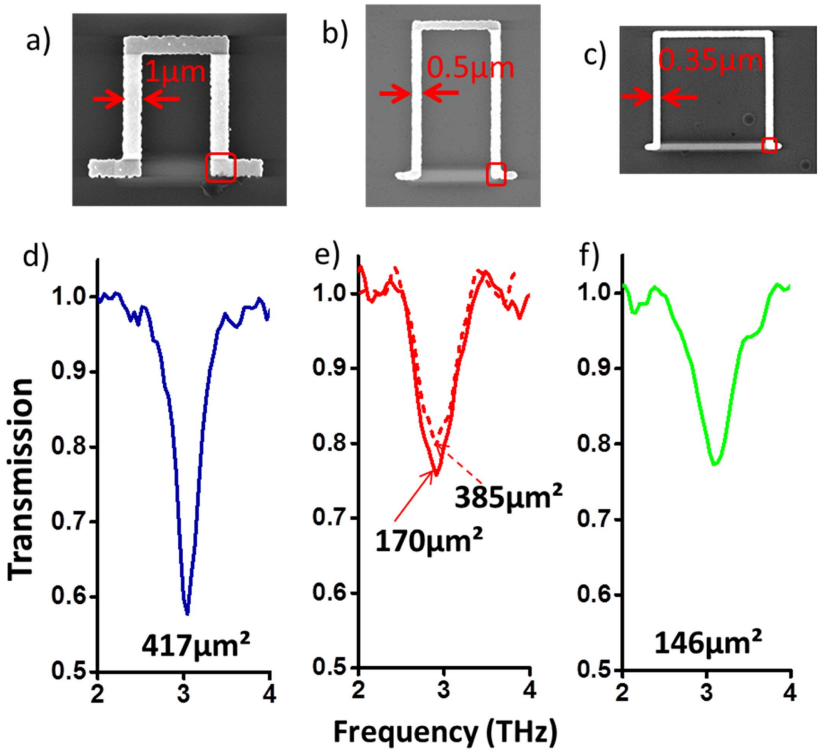

Figure 5. (a)–(c) Scanning electron microscope pictures of circuit resonators realized with SiO_2 layer of thickness L. For each figure, the side of the square capacitive parts is equal to the widths of the upper metallic part for the indicated values. The other dimensions of the resonators are respectively: (a) $L = 1$ μm and 6 μm $\times$ 4 μm (internal length times internal width of the square loop), (b) $L = 0.5$ μm and 8 μm $\times$ 4 μm; (c) $L = 0.25$ μm and 6 μm $\times$ 6 μm. (d)–(f): reflectivity spectra on arrays of LC resonators. The spectrum corresponds to the structure indicated above. The array unit cell surface Σ is indicated for each spectrum.

Table 1. Effective volume V_{eff} (obtained by finite difference domain software) and geometrical volume V for LC structures with different capacitative area. Ψ is a correction factor as a consequence of the intersubband selection rule.

Structure	V_{eff} (μm^3)	Ψ	V_{eff}/Ψ (μm^3)	$V = 2\sigma L$ (μm^3)
1×1 μm^2	0.7	0.72	0.97	2
0.5×0.5 μm^2	0.2	0.72	0.28	0.25
0.35×0.35 μm^2	0.047	0.66	0.071	0.061

pictures of the structures are shown in figures 5(a)–(c), and the corresponding optical characterizations are presented in figures 5(d)–(f). The cross section of the capacitive part was respectively $\sigma = 1 \times 1$ μm^2, 0.5×0.5 μm^2 and 0.35×0.35 μm^2. The dielectric slab thickness was respectively $L = 1$ μm, 0.5 μm and 0.25 μm. The spectra presented in figures 5(d)–(f) are transmission spectra, for the indicated array unit area Σ. For the 0.5×0.5 μm^2 structure (figure 5(b)) we measured arrays with two different Σ as indicated in figure 5(e). The collection area for these systems that have both transmission and reflection ports is now defined as $A_{\text{coll}} = \Sigma(1 - \mathscr{R}_{\text{min}} - \mathscr{T}_{\text{min}})$ in a straightforward generalization of equation (9). In our structures, we observed no features in the reflectivity port ($R_{\text{min}} = 0$) and therefore $A_{\text{coll}} = \Sigma(1 - \mathscr{T}_{\text{min}})$.

In order to estimate the effective volumes of our structures, we simulated the electromagnetic field by using finite difference domain software. The effective volume of the electric field was estimated as $V_{\text{eff}} = \int w_e \, dV / \max(w_e)$, where w_e is the time-averaged electric energy density. To take into account the intersubband selection rule, this quantity was corrected with a factor $1/\Psi$, defined as $\Psi = \int |E_z|^2 dV \Big/ \int (|E_x|^2 + |E_y|^2 + |E_z|^2) dV$. The values obtained for the effective volume V_{eff}/Ψ are thus used for the estimation of the focusing factor in equation (7). The numerical results are summarized in table 1, in comparison with the geometrical volume $V = 2\sigma L$.

The focusing factors F for both patch cavities and LC-resonators is presented in figure 6(a) as a function of the array cross section Σ. Even if the microcavities and LC resonators studied for this plot operate at different THz frequencies, we expect that the orders of magnitude of the focusing factors will be the same. For the patch

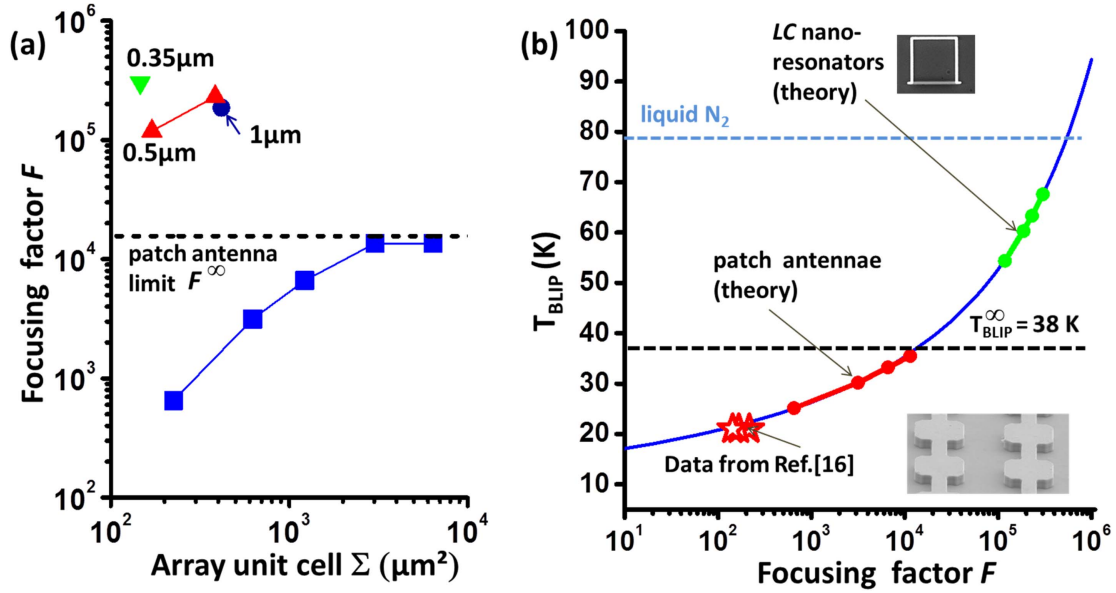

Figure 6. (a) A summary of the focusing factors F from arrays of nano-resonators with different geometries discussed in this work. The squares are the rectangular patches and the other symbols indicate the LC resonators described in figure 5, with the corresponding size of the square capacitance. This figure combines data with structures that operate from 3 to 5 THz, assuming that the dependence of F on the frequency is weak in the spectral range. The dashed line is the limit for patch antennas from equation (13). (b) T_{BLIP} as a function of the focusing factor F (continuous line). The line+symbols curves correspond to the different resonators discussed in this work, and the dashed line to the patch antenna limit. The stars corresponds to experimental values reported in [16].

cavities we have indicated the single resonator limit from equation (13), that is independent from the operating wavelength, as the quality factors in such systems do not change significantly from 3 THz to 5 THz. We observe that the *LC* structures have systematically higher focusing factors F than the patch cavities, even for dense arrays with small Σ. According to our results for the evolution of A_{coll} as a function of Σ (figure 2(d)), even higher focusing factors should be expected in low density arrays.

In figure 6(b) we show the expected elevation of the BLIP temperature as a function of the focusing factor F (equation (5)) for the THz detector from [16]. The continuous curve is a numerical result obtained from equation (6). The stars correspond to the experimental data from [16]. The projected T_{BLIP} for the LC circuits, even in dense arrays is above 70 K, while the limit for the patch-cavity systems is $T^{\infty}_{BLIP} = 38$ K. Capacitive parts with widths as small as 100 nm are feasible by electrical lithography. This resonator architecture therefore could allow reaching operating temperatures close to the liquid Nitrogen temperature. Clearly, this concept will be beneficial also for Mid-IR detectors where the T_{BLIP} temperature could reach 130 K from $T^{0}_{BLIP} = 70$ K.

Another important figure of merit that can be impacted by the architecture of the resonators is the specific detectivity, which should be redefined appropriately. Since we expect the effect of the dark current to be reduced in our architectures, we are going to consider the background limited specific detectivity D^{*}_{BLIP}. We use the following definition:

$$D^{*}_{BLIP} = \frac{R\sqrt{A_{coll}}}{\sqrt{4eg\,(I_{photo} + I_{dark}\,(T))}} \tag{14}$$

Here, differently from the standard definition in [32, 36] the specific detectivity has been normalized on the collection area A_{coll} instead of the area of the device σ. This choice is justified as follows: at low temperature, the dark current is negligible, and the main source of noise in the detector is the photocurrent I_{photo}. Then, using equation (1), we can express the specific detectivity at low temperature:

$$D^{*}_{BLIP}(\mathrm{T} = 0\mathrm{K}) = \frac{\sqrt{R}}{\sqrt{4egE_{21}\Phi_{300K}}}, \tag{15}$$

with $\Phi_{300\mathrm{K}}$ the number of photons per unit surface and per unit time radiated by a black-body at the peak absorption energy E_{21} of the detector. In equation (15), the specific detectivity becomes independent of the collection area A_{coll}, as required for the standard definition. The responsivity entering this formula is the internal responsivity defined in equation (3). In figure 7, we have plotted the predictions from equation (14) for the different THz devices envisioned in this work and [16]. The maximum detectivities at low temperature have been computed from the experimental data reported in [16]. The first feature that is clearly visible is the increase of the temperature performance of the detector through the higher T_{BLIP} as discussed above. In accordance with

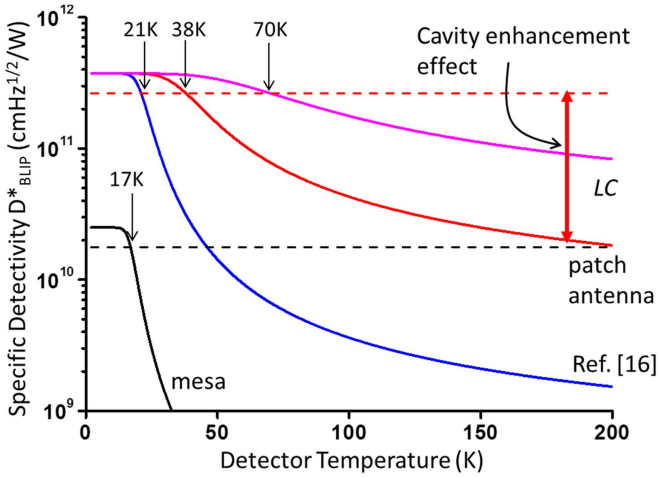

Figure 7. Background limited specific detectivity D^* as a function of the temperature, for the case of different structures presented in this work. The maximum value of D^* depends only on the vertical confinement of the structure, expressed as the ratio λ_{21}/L ('cavity enhancement effect'). An increased focusing factor F leads to an increase in the temperature range of the detector operation through an increased T_{BLIP}.

equations (1), (2) and (14) the T_{BLIP} corresponds to the temperature where the detectivity is less than a factor of $2^{1/2}$ than its maximal value (dashed lines in figure 6). While the T_{BLIP} is increased, the decrease of the specific detectivity with the temperature is also slowed down, meaning that the detector can operate efficiently at temperature higher than T_{BLIP}. For these plots, we have assumed that the gain g and the absorption coefficient B_{isb} of the detector are constant as a function of the temperature. Note that this hypothesis is a simplification since the gain can exhibit temperature dependence [62] and the absorption coefficient decreases with the temperature due to thermal redistribution of carriers [63].

Another impact of the cavity geometry that is visible in figure 6 is the increase of the maximum detectivity with respect to the mesa device. This increase can be explained by considering equation (5), which links the absorption coefficient in the cavity geometry (B_{isb}) with that the quantum efficiency in the mesa geometry (λ). The absorption coefficient is enhanced due to the ratio λ_{21}/L, which expresses the vertical confinement in the cavity. Indeed, this factor is higher for structures with highly sub-wavelength thickness ($L \ll \lambda_{21}$), which results to higher responsivities for the cavity geometry with respect to the mesa [16].

It is interesting to note that our results provide a theoretical limit for the maximum achievable background limited detectivity in a microcavity-coupled system. Indeed, using the expression (3) for the case, $B_{isb} \gg 1/Q_{cav}$, and replacing the resulting expression for the responsivity in equation (15), we obtain:

$$D^*_{BLIP}(\mathrm{T} = 0\mathrm{K}) \leqq \frac{1}{E_{21}\sqrt{2N_{qw}\Phi_{300K}}} \tag{16}$$

This results states that the maximum BLIP specific detectivity is optimized in detectors which contain a single quantum well, $N_{qw} = 1$ which absorbs most of the photons fed in the cavity. In that case, the photon flux from the thermal background coupled in the detector Φ_{300K} depends only on the energy (Planck's radiation law) and the spectral bandwith of the detector. The maximum BLIP detectivity is then provided solely by the absorption energy of the detector E_{21} and the spectral width of the responsivity curve, as the only source of noise in the system are the carriers generated by the photons from the 300 K background. A typical value estimated from equation (16) for a THz detector operating at 5.4 THz with a single quantum well and 10% spectral bandwidth is $D^*_{BLIP} = 6 \times 10^{12}$ cmHz$^{1/2}$/W. Note that this value does not limit the dark current-limited detectivity D^*_{signal}, which is expected to increase with the ratio $(A_{coll}/\sigma)^{1/2}$ [27]. This corresponds to a situation where the detector is shielded from the thermal radiation and is illuminated only by the source to be measured.

In summary, we have studied the impact of the lateral and vertical photonic confinement for quantum detectors of infrared radiation. We have pointed out the importance of two figures of merit, the collection area of the detector A_{coll} and a dimensionless local field enhancement factor F. We have shown how the collection area A_{coll} can be inferred directly from reflectivity measurements on arrays of nano-resonators. We also commented the effect of such array configuration on the detector performance, taking into account the finite size of the incident beam. Namely, there is always a trade-off between the collection efficiency of the detector array and its temperature performance. We linked the maximum background limited operating temperature T_{BLIP} to the local field enhancement factor F, which has been expressed in equation (7) through A_{coll}, the quality factor of the structure Q and the volume V. We have found that in systems such as patch microcavities, which rely on

propagation effects, F is ultimately limited by the resonator loss. This limit can be exceeded in electromagnetic resonators based on quasi-static effects, such as LC circuits. In particular, our theoretical predictions indicate that THz detectors based on such resonators would operate close to the liquid nitrogen temperature. The figures of merit A_{coll} and F introduced here can also be applied to other systems which provide highly subwavelength confinement, such as, for instance, the localized plasmon modes in metallic nano-particles [64]. As another example, we expect very strong high order non-linear effects proportional to F^2 or F^3, due to the very tight field confinement in these nanostructures [65].

Acknowledgements

We acknowledge financial support from the FP7 ITN NOTEDEV project (Grant No. 607521).

References

[1] Novotny L and Van Hulst N 2011 *Nat. Photon.* **5** 83–90
[2] Schuller J A, Barnard E S, Cai W, Jun Y C, White J S and Brongersma M L 2010 *Nat. Mater.* **9** 193–204
[3] Atwater H A and Polman A 2010 *Nat. Mater.* **9** 205–13
[4] Biagioni P, Huang J-S and Hecht B 2012 *Rep. on Prog. Phys.* **75** 024402
[5] Berkovitch N, Ginzburg P and Orenstein M 2012 *J. Phys. Condens. Matter* **24** 073202
[6] Aksu S, Yanik A A, Adato R, Artar A, Huang M and Altug H 2010 *Nano Lett.* **10** 2511–8
[7] Todorov Y, Tosetto L, Teissier J, Andrews A, Klang P, Colombelli R, Sagnes I, Strasser G and Sirtori C 2010 *Opt. Express* **18** 13886
[8] Feuillet-Palma C, Todorov Y, Vasanelli A and Sirtori C 2013 *Sci. Rep.* **3** 1361
[9] Lee B, Lee I M, Kim S, Oh D H and Hesselink L 2010 *J. Mod. Opt.* **57** 1479–97
[10] Schwarz S E and Ulrich B T 1977 *J. Appl. Phys.* **48** 1870–3
[11] Tang L, Kocabas S E, Latif S, Okyay A K, Ly-Gagnon D S, Saraswat K C and Miller D A 2008 *Nat. Photon.* **2** 226–9
[12] Kim S, Zimmerman J D, Focardi P, Gossard A C, Wu D H and Sherwin M S 2008 *Appl. Phys. Lett.* **92** 253508
[13] Rice J P, Grossman E N and Rudman D A 1994 *Appl. Phys. Lett.* **65** 773–5
[14] Vicarelli L, Vitiello M S, Coquillat D, Lombardo A, Ferrari A C, Knap W, Polini M, Pellegrini V and Tredicucci A 2012 *Nat. Mater.* **11** 865–71
[15] Chen Y N, Todorov Y, Askenazi B, Vasanelli A, Biasiol G, Colombelli R and Sirtori C 2014 *Appl. Phys. Lett.* **104** 031113
[16] Palaferri D, Todorov Y, Chen Y N, Madeo J, Vasanelli A, Li L H, Davies A G, Linfield E H and Sirtori C 2015 *Appl. Phys. Lett.* **106** 161102
[17] Cao L, Park J S, Fan P, Clemens B and Brongersma M 2010 *Nano Lett.* **10** 1229–33
[18] Fan P, Huang K C Y, Cao L and Brongersma M 2013 *Nano Lett.* **13** 392–6
[19] Fan P, Chettiar U, Cao L, Afshinmanesh F, Engheta N and Brongersma M 2012 *Nat. Photon.* **6** 380–5
[20] Kinkhabwala A, Yu Z, Fan S, Avlasevich Y, Mullen K and Moerner W 2009 *Nat. Photonics* **3** 654
[21] Curto A, Volpe G, Taminiau T, Kreuzer M, Quidant R and Van Hulst N 2010 *Science* **329** 930
[22] Taminiau T, Stefani F, Segerink F and Van Hulst N 2008 *Nat. Photon.* **2** 234
[23] Madeo J, Todorov Y and Sirtori C 2014 *Appl. Phys. Lett.* **104** 031108
[24] Bohren C F 1983 *Am. J. Phys.* **51** 323
[25] Frenkel I 1955 Principles of the Theory of Atomic Nuclei *Isd. Akad. Nauk SSSR Moscow* p 193
[26] Balanis C A 2005 *Antenna Theory* (New York: John Wiley & Sons.)
[27] Martyniuk P, Antoszewski J, Martyniuk M, Faraone L and Rogalski A 2014 *Appl. Phys. Rev.* **1** 041102
[28] Sverdlov B N, Botchkarev A E, Teraguchi N and Salvador A 1993 *Electron. Lett.* **29** 1019–21
[29] Kim J P and Sarangan A M 2006 *Appl. Opt.* **45** 6065–70
[30] Kalchmair S *et al Opt. Express* 2012 **20** 5622
[31] Orfanidis S J *Electromagnetic Waves and Antennas* (Piscataway, NJ: Rutgers University) (http://ece.rutgers.edu/~orfanidi/ewa/)
[32] Rosencher E and Vinter B (ed) 2004 *Optoelectronics* (Cambridge: Cambridge University Press)
[33] Gunapala S, Bandara S, Singh A, Liu J, Luong E, Mumolo J and LeVan P 2000 *Physica* E **7** 108
[34] Gunapala S, Bandara S, Liu J, Luong E, Rafol S, Mumolo J, Ting D, Bock J, Ressler M and Werner M 2001 *Infrared Phys. Technol.* **42** 267
[35] Luo H, Liu H C, Song C Y and Wasilewski Z R *Appl. Phys. Lett.* **86** 231103
[36] Schneider H and Liu H C 2007 *Quantum Well Infrared Photodetectors* (Berlin: Springer)
[37] Zhang S, Wang T M, Hao M R, Yang Y, Zhang Y H, Shen W Z and Liu H C 2013 *J. Appl. Phys.* **114** 194507
[38] Helm M 2000 *The Basic Physics of Intersubband Transitions in Intersubband Transitions in Quantum Wells Physics and Device Applications* ed H C Liu and F Capasso vol 1 (San Diego, CA: Academic) pp 212–452
[39] Seok T J *et al* 2011 *Nano Lett.* **11** 2606–10
[40] Liu H C, Dudek R, Shen A, Dupont E, Song C Y, Wasilewski Z R and Buchanan M 2001 *Appl. Phys. Lett.* **79** 4237
[41] Guo X G, Zhang R, Liu H C, SpringThorpe A J and Cao J C 2010 *Appl. Phys. Lett.* **97** 021114
[42] Collin S 2014 *Rep. Prog. Phys.* **77** 126402
[43] Singh R, Rockstuhl C and Zhang W 2010 *Appl. Phys. Lett.* **97** 241108
[44] Bitzer A, Wallauer J, Helm H, Merbold H, Feurer T and Walther M 2009 *Optics Express* **17** 22108
[45] Feuillet-Palma C, Todorov Y, Steed R, Vasanelli A, Biasiol G, Sorba L and Sirtori C 2012 *Opt. Express* **20** 29121
[46] Jouy P, Todorov Y, Vasanelli A, Colombelli R, Sagnes I and Sirtori C 2011 *Appl. Phys. Lett.* **98** 021105
[47] González F J, Gritz M A, Fumeaux C and Boreman G D 2002 *Int. J. Infrared Millim. Waves* **23** 785–97
[48] Gonzalez F J, Ilic B, Alda J and Boreman G D 2005 *IEEE Journal of Selected Topics in Quantum Electronics* **11** 117–20
[49] Strupiechonski E, Xu G, Cavalié P, Isac N, Dhillon S, Tignon J, Beaudoin G, Sagnes I, Degiron A and Colombelli R 2013 *Phys. Rev.* B **87** 041408 (R)
[50] Paulillo B, Manceau J M, Degiron A, Zerounian N, Beaudoin G, Sagnes I and Colombelli R 2014 *Opt. Express* **22** 21302–12
[51] Paulillo B, Manceau J M, Li L H, Davies A G, Linfield E H and Colombelli R 2016 *Appl. Phys. Lett.* **108** 101101
[52] Shalaev V M 2007 *Nat. Photon.* **1** 41–8

[53] Feynman R P, Leighton R B and Sands M 1977 *The Feynman Lectures on Physics: Mainly Electromagnetism and Matter* vol 2 (Oxnard, CA: Addison-Wesley)
[54] Walther C, Scalari G, Amanti M I, Beck M and Faist J 2010 *Science* **327** 1495–7
[55] Dietze D, Benz A, Strasser G, Unterrainer K and Darmo J 2011 *Opt. Express* **19** 13700
[56] Strupiechonski E *et al* 2012 *Appl. Phys. Lett.* **100** 131113
[57] Benz A, Campione S, Liu S, Montaño I, Kleim J F, Allerman A, Wendt J R, Sinclair M B, Capolino F and Brener I 2013 *Nat. Comm.* **4** 2882
[58] Benz A, Montaño I, Klem J F and Brener I 2013 *Appl. Phys. Lett.* **103** 263116
[59] Todorov Y, Desfond P, Belacel C, Becerra L and Sirtori C 2015 *Opt. Express* **23** 16838–45
[60] Benz A, Campione S, Klem J F, Sinclair M B and Brener I 2015 *Nano Lett.* **15** 1959–66
[61] Todorov Y and Sirtori C 2014 *Phys. Rev.* X **4** 041031
[62] Goldberg A C, Little J W, Kennerly S W, Beekman D W and Leavitt R P 1999 Temperature dependence of the responsivity of quantum well infrared photodetectors *Proc. 6th Int. Symp. LWIR Detectors and Arrays: Physics and Applications* **98** (Boston, MA: Electrochemical Society) pp 122–3
[63] Todorov Y, Tosetto L, Delteil A, Vasanelli A, Andrews A M, Strasser G and Sirtori C 2012 *Phys. Rev.* B **86** 125314
[64] Khurgin J B 2015 *Nat. Nanotechnol.* **10** 2–6
[65] Maier S A 2006 *Opt. Express* **14** 1957–64